Computation of Three-Dimensional Turbulent Vortical Flows on Bodies at High Incidence

Lewis B. Schiff,* David Degani,† and Russell M. Cummings‡
NASA Ames Research Center, Moffett Field, California 94035

As Navier-Stokes computations are carried out for high-angle-of-attack flows, the various numerical and physical factors affecting the accuracy of the flow predictions must be determined. In an effort to further this understanding, numerical predictions of the complex three-dimensional separated flow about bodies of revolution in supersonic and subsonic flows have been performed. Predictions have been made for the supersonic flow over a secant ogive cylinder at relatively low angles of attack using a thin-layer Navier-Stokes code, showing good agreement with experimental pressure measurements as well as boundary-layer velocity profiles. The predictions are also compared with parabolized Navier-Stokes computations from a previous work. Subsonic predictions at high angles of attack were made for a tangent ogive cylinder and were found to be in good agreement with available experimental data. The accuracy of the predictions are shown to depend on using grids that are sufficiently fine to resolve the details of both the viscous boundary layer and the off-surface separated flow structures and, for turbulent flow cases, the use of a turbulence model that accounts for the leeward vortical flow structures. An example of high-incidence flow computed about a more complex geometry, the F-18 fighter fuselage forebody and leading-edge extension, is also presented.

I. Introduction

COMPUTATION of flow over bodies at large angles of attack is a difficult, but significant, problem in aerodynamics. High-angle-of-attack flow is governed by large regions of three-dimensional separated flow, where the boundary layers leave the surface of the body along lines of separation, and roll up on the leeward side of the body to form strong, concentrated vortical flows. Separated flows have historically been treated by a wide variety of computational methods ranging from potential flow methods, vortex cloud methods, inviscid panel methods incorporating free shear layers, Euler methods, and most recently, parabolized Navier-Stokes (PNS) and time-marching Navier-Stokes techniques. In addition, a variety of combined inviscid/viscous techniques (potential/boundary layer or Euler/boundary-layer techniques) have been utilized. However, the close coupling that exists between the strength and location of the leeward vortical flow and the location of the viscous layer separation lines has precluded accurate predictions of high-incidence flow with the more approximate techniques. Consequently, we have focused solely on PNS and time-marching Navier-Stokes computations.

The introduction of recent supercomputers such as the CRAY-2 has permitted a quantum increase in the size of computational grids. As a result, it is now possible to compute high-angle-of-attack flows over bodies and aircraft components with codes based on the Reynolds-averaged Navier-Stokes equations and use sufficient grid points to adequately resolve the main features of the three-dimensional separated flowfield (cf., Refs. 1-8).

In previous work, Schiff and Sturek[9] and Degani and Schiff[10,11] have compared results for supersonic viscous flow, obtained using a PNS method,[12] to experimental measurements. In Ref. 9, it was shown that the PNS predictions were in good agreement with experimental data at low angles of attack, with the accuracy of the predictions diminishing at higher incidence angles. In Refs. 10 and 11, predictions were performed using a PNS code, and it was shown that accurate computation of high-angle-of-attack supersonic flow can be achieved by 1) use of grid resolutions adequate to resolve the details of both the viscous boundary layers and the off-surface vortical flow, and 2) for turbulent flows, use of an eddy-viscosity turbulence model that properly accounts for the leeward vortical flow structure. The ability of the PNS code to accurately predict high-incidence flow has also been tested on other geometries such as cones and prolate spheroids with good results.

In the current work, we apply a time-marching thin-layer Navier-Stokes (TLNS) code, reported by Steger et al.,[13] to compute laminar and turbulent flow over bodies at large angles of attack. The code was first calibrated by comparing solutions for supersonic flow over an ogive-cylinder body at $M_\infty = 3.0$ with solutions obtained from the PNS method and with available experimental data. The code was then used to compute a series of laminar and turbulent flows over a longer ogive cylinder in subsonic flow at $M_\infty = 0.2$. Finally, predictions are made for a more complex geometry, the F-18 fuselage forebody, in order to assess the ability of the prediction methodology to predict high-incidence flow for aircraft.

II. Theoretical Background

Governing Equations

The conservation equations of mass, momentum, and energy can be represented in a flux-vector form that is convenient for numerical simulation as[14]

$$\partial_\tau \hat{Q} + \partial_\xi(\hat{F} + \hat{F}_v) + \partial_\eta(\hat{G} + \hat{G}_v) + \partial_\zeta(\hat{H} + \hat{H}_v) = 0 \qquad (1)$$

where τ is the time, and the independent spatial variables ξ, η, and ζ are chosen to map a curvilinear body-conforming grid into a uniform computational space (see Fig. 1). In Eq. (1),

Received Jan. 16, 1990; revision received Oct. 9, 1990; accepted for publication Nov. 9, 1990.

*Special Assistant for High Alpha Technology, Fluid Dynamics Division. Associate Fellow AIAA.

†National Research Council Associate; Associate Professor, on leave from Faculty of Mechanical Engineering, Technion IIT, Haifa, Israel. Associate Fellow AIAA.

‡National Research Council Research Associate; Associate Professor, on leave from Aeronautical Engineering Department, California Polytechnic State University, San Luis Obispo, CA. Associate Fellow AIAA.

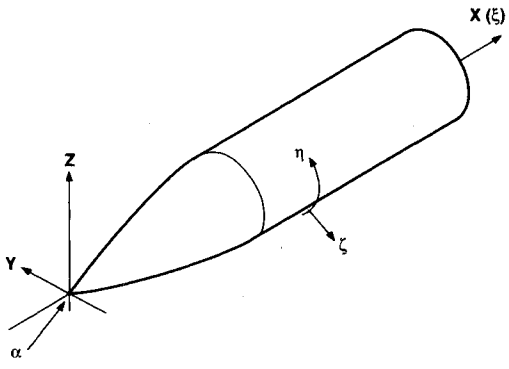

Fig. 1 Coordinates and notation.

$\hat{Q}$ is the vector of dependent flow variables; $\hat{F} = \hat{F}(\hat{Q})$, $\hat{G} = \hat{G}(\hat{Q})$, and $\hat{H} = \hat{H}(\hat{Q})$ are the inviscid flux vectors; and $\hat{F}_v$, $\hat{G}_v$, and $\hat{H}_v$ are fluxes containing the viscous derivatives. A nondimensional form of the equations is used throughout this work. The conservative form of the equations is maintained chiefly to capture the Rankine-Hugoniot shock jump relations (where applicable) as accurately as possible.

For body-conforming coordinates and high Reynolds number flow, if ζ is the coordinate leading away from the surface, the thin-layer approximation can be applied, which yields[15,16]

$$\partial_\tau \hat{Q} + \partial_\xi \hat{F} + \partial_\eta \hat{G} + \partial_\zeta \hat{H} = Re^{-1} \partial_\zeta \hat{S} \tag{2}$$

where only viscous terms in ζ are retained. These have been collected into the vector $\hat{S}$, and the nondimensional Reynolds number Re is factored from the viscous flux term.

In differencing these equations, it is often advantageous to difference about a known base solution denoted by subscript o as follows

$$\begin{aligned} &\delta_\tau(\hat{Q} - \hat{Q}_o) + \delta_\xi(\hat{F} - \hat{F}_o) + \delta_\eta(\hat{G} - \hat{G}_o) \\ &\quad + \delta_\zeta(\hat{H} - \hat{H}_o) - Re^{-1}\delta_\zeta(\hat{S} - \hat{S}_o) \\ &\quad = -\partial_\tau \hat{Q}_o - \partial_\xi \hat{F}_o - \partial_\eta \hat{G}_o - \partial_\zeta \hat{H}_o + Re^{-1}\partial_\zeta \hat{S}_o \end{aligned} \tag{3}$$

where δ indicates a general difference operator, and ∂ is the differential operator. If the base state is properly chosen, the differenced quantities can have smaller and smoother variation and, therefore, less differencing error. In particular, errors introduced into the solution by the finite difference approximations of the spatial metrics can be reduced. In the current application, the freestream is used as the base solution and the right-hand side of Eq. (3) is zero.

Numerical Algorithm

The implicit scheme employed in this study is the F3D algorithm reported by Steger et al.[13] The algorithm uses flux-vector splitting[17] and upwind spatial differencing for the convection terms in one coordinate direction (nominally streamwise). As discussed in Ref. 13, schemes using upwind differencing can have several advantages over methods that utilize central spatial differences in each direction. In particular, such schemes can have natural numerical dissipation and better stability properties. By using upwind differencing for the convective terms in the streamwise direction while retaining central differencing in the other directions, a two-factor implicit approximately factored algorithm is obtained, which is unconditionally stable[18] for a representative model wave equation. The scheme may be written for the TLNS equations in the form

$$\begin{aligned} &[I + h\delta_\xi^b(\hat{A}^+)^n + h\delta_\zeta \hat{C}^n - hRe^{-1}\bar{\delta}_\zeta J^{-1}\hat{M}^n J - D_i|_\zeta] \\ &\quad \times [I + h\delta_\xi^f(\hat{A}^-)^n + h\delta_\eta \hat{B}^n - D_i|_\eta]\Delta\hat{Q}^n \\ &\quad = -\Delta t\{\delta_\xi^b[(\hat{F}^+)^n - \hat{F}_\infty^+] + \delta_\xi^f[(\hat{F}^-)^n - \hat{F}_\infty^-] \\ &\quad + \delta_\eta(\hat{G}^n - \hat{G}_\infty) + \delta_\zeta(\hat{H}^n - \hat{H}_\infty) \\ &\quad - Re^{-1}\bar{\delta}_\zeta(\hat{S}^n - \hat{S}_\infty)\} - D_e(\hat{Q}^n - \hat{Q}_\infty) \end{aligned} \tag{4}$$

where $h = \Delta t$ or $\Delta t/2$ for first- or second-order time accuracy, and the freestream base solution is used. Second-order time accuracy is used when a nonsteady solution is required. In Eq. (4), δ is typically a three-point, second-order-accurate, central difference operator, $\bar{\delta}$ is a midpoint operator used with the viscous terms, and the operators δ_ξ^b and δ_ξ^f are backward and forward three-point difference operators. The flux $\hat{F}$ has been split into $\hat{F}^+$ and $\hat{F}^-$, according to its eigenvalues,[17] and the matrices $\hat{A}^\pm$, $\hat{B}$, $\hat{C}$, and $\hat{M}$ result from local linearization of the fluxes about the previous time level. J denotes the Jacobian of the coordinate transformation. Dissipation operators D_e and D_i are used in the central space differencing directions. Full details of the development of the algorithm may be found in Refs. 13 and 18.

Numerical Smoothing

The finite difference scheme uses flux splitting in the ξ direction and central differencing in the η and ζ directions. As a consequence, numerical dissipation terms denoted by D_i and D_e in Eq. (4) are employed in the η and ζ directions and are given as combinations of second and fourth differences. The smoothing terms are of the form

$$D_e|_\eta = (\Delta t)J^{-1}\{\epsilon_2\bar{\delta}|\hat{B}|\beta\bar{\delta} + \epsilon_4\bar{\delta}\frac{|\hat{B}|}{1+\beta}\bar{\delta}^3\}|_\eta J \tag{5a}$$

$$D_i|_\eta = (\Delta t)J^{-1}\{\epsilon_2\bar{\delta}|\hat{B}|\beta\bar{\delta} + 2.5\epsilon_4\bar{\delta}\frac{|\hat{B}|}{1+\beta}\bar{\delta}^3\}|_\eta J \tag{5b}$$

where

$$\beta = \frac{|\bar{\delta}^2 p|}{|(1+\bar{\delta}^2)p|}$$

and where $|\hat{B}|$ is the absolute value of the matrix $\hat{B}$ or an approximation. Here, p is the nondimensional fluid pressure and ϵ_2 is $\mathcal{O}(1 + M_\infty^2)$, whereas ϵ_4 is $\mathcal{O}(0.01)$. In this form, the second-order smoothing terms act to control numerical oscillations across shock waves, whereas the fourth-order smoothing is effective elsewhere. In order to improve the accuracy of the solutions, the fourth-order numerical smoothing terms are further scaled by q/q_∞. This has the effect of reducing the numerical smoothing in the viscous layer adjoining the body surface where viscous dissipation controls the dispersion and where additional numerical smoothing terms can adversely affect the accuracy of the solution by modifying the physical viscous terms. The effect of numerical experiments in which the magnitude of the added fourth-order smoothing terms were varied are described in a later section.

Boundary Conditions and Initial Conditions

Supersonic Cases

Both PNS space-marching and TLNS time-marching solutions were obtained for the supersonic cases in order to compare the TLNS solutions against the well-established PNS results. The PNS solutions were obtained for a 6-diameter secant ogive-cylinder body ($D = 0.1875$ ft) using the PNS code developed by Schiff and Steger.[12] The grid used is shown schematically in Fig. 2. An initial conical solution was obtained at $x = 0.050$ feet using the marching/step-back procedure described in Ref. 9, and the solution was marched downstream to $x = 1.130$ ft with $\Delta x = 0.0025$ ft, resulting in 433 axial planes including the initial and final data planes. In each axial plane, the grid contained 50 radial points and 72 circumferential points ($\Delta\phi = 5$ deg), which extended circumferentially completely around the body. An implicit periodic con-

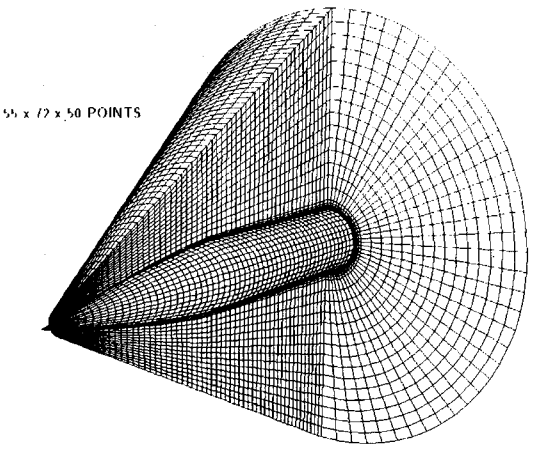

Fig. 2 Secant ogive-cylinder grid.

tinuation condition was used at the circumferential edges of the grid. At the body surface, an adiabatic no-slip boundary condition was imposed, whereas undisturbed freestream conditions were imposed at the computational outer boundary.

The grid utilized for supersonic TLNS computations consisted of every eighth axial plane of the PNS grid, resulting in a grid of 55 axial planes. Further, the computed supersonic flows were found to be symmetric about the angle-of-attack plane. Thus, for the supersonic TLNS computations, only half of the PNS grid was used. This resulted in a grid having 55 axial, 50 radial, and 39 circumferential points ($\Delta\phi = 5$ deg). The PNS solution was used as the initial data for the TLNS time-marching code, and the solution was advanced in time until a steady solution was obtained. In these time-marching computations, the upstream data plane was held fixed for all time at the PNS conical solution. An adiabatic no-slip condition was applied at the body surface, and undisturbed freestream conditions were imposed at the outer boundary. An implicit symmetry plane boundary condition was imposed at the circumferential edges of the grid, whereas at the downstream boundary a simple zero-axial-gradient extrapolation condition was applied.

Subsonic Cases

For subsonic TLNS computations, a grid similar to the one shown schematically in Fig. 3 was utilized. The no-slip wall boundary condition, the undisturbed freestream boundary condition, and the implicit symmetry plane condition are identical to those used for the supersonic cases, as is the zero-gradient extrapolation outflow condition. The simple extrapolation boundary condition is not strictly valid in subsonic flow since the body wake can affect the flow on the body. However, by letting the computed body length extend beyond the physical length of the body, and neglecting the portion of the flow near the downstream boundary, we can minimize the effect of the boundary. The outflow boundary extends 4.5 diameters downstream of $x/D = 6.0$, whereas the inflow and upper boundaries extend 8 and 11 diameters from the body, respectively. On the upstream axis of symmetry, an extrapolation boundary condition was used to obtain the flow conditions on the axis from the cone of points one axial plane downstream. The flowfield was initially set to freestream conditions throughout the grid and was advanced in time until a steady solution was obtained. The flowfield was assumed to be symmetric and a half-body grid was used.

Turbulence Model

The coefficients of viscosity and thermal conductivity that appear in Eq. (2) are specified from auxiliary relations. For laminar flow, the coefficient of viscosity is obtained using Sutherland's law, whereas for turbulent flow, the coefficient is obtained from the eddy-viscosity turbulence model reported by Degani and Schiff.[10,11] The coefficient of thermal conductivity is obtained once the viscosity coefficient is known by assuming a constant Prandtl number.

Degani and Schiff[10,11] developed a modification to the well-known Baldwin-Lomax[15] model (which is, in turn, based on the two-layer model reported by Cebeci et al.[19]). The modifications extend the model in a rational manner to permit an accurate determination of the viscous length scale for high-angle-of-attack flows in regions of crossflow separation, where a strong leeward vortical flow structure exists.

As proposed by Baldwin and Lomax,[15] the turbulence model examines a quantity containing the local fluid vorticity magnitude to determine the length scale and, thus, the eddy-viscosity coefficient. The modifications made by Degani and Schiff[10,11] permit the model to differentiate between the vorticity within the attached boundary layers from the vorticity on the surfaces of separation and, thus, to select a length scale based on the thickness of the attached boundary layers rather than one based on the radial distance between the body surface and the surface of separation. The latter scale length can be much greater than that based on the boundary-layer thickness, and if used, the resulting eddy-viscosity coefficient can be as much as two orders of magnitude too high. In general, this will cause the primary vortices to be smaller than those observed experimentally, and the primary separation line will be located closer to the leeward symmetry plane. In addition, the secondary (and tertiary) separation lines will not occur in the computed flows. Details of the implementation of the modifications to the model can be found in Refs. 10 and 11. An illustration of the differences between a high-incidence subsonic flow computed with and without the modifications is presented in a later section.

III. Results and Discussion

In an effort to predict flows around bodies at high angles of attack, it is necessary to determine the factors, both numerical and physical, that are essential for accurate and robust solutions. Although there may be numerous factors affecting the results of the numerical predictions, several factors have been found to be extremely important for highly separated flows.

Supersonic High-Incidence Flow

In order to gain confidence in the ability of the TLNS code to accurately compute high Reynolds number flows, TLNS results were compared with results obtained with the PNS code[12] for flow over a 6-diameter-long secant ogive-cylinder body. PNS solutions computed for turbulent flow over this body at $M_\infty = 3.0$, $Re_D = 1.216 \times 10^6$, and $\alpha = 4.2$, 6.3, and 10.4 deg had previously been compared to experimental measurements[20,21] in Refs. 10 and 11. The PNS solutions were recomputed and used as initial conditions for the TLNS code, which was then run to convergence. As mentioned earlier, in each axial plane, the TLNS grid contained 50 radial and 39 circumferential planes ($\Delta\phi = 5$ deg). This grid resolution had been previously found adequate,[9-11] even for the $\alpha = 10.4$ deg case in which crossflow separation was present. In both codes, turbulence was modeled using the modified eddy-viscosity model described in Refs. 10 and 11. For the current computations, the turbulence model coding was modified to obtain computer vectorization and to compute the eddy viscosity at the grid points (rather than midway between adjacent radial points, as had been done previously).

Effect of Smoothing Terms

Initial comparisons for the $\alpha = 4.2$ deg case (not presented) showed very good agreement between the pressure fields computed with both codes and with the experimentally measured pressures.[20] However, a discrepancy was observed between the computed surface shear stress values. A series of numerical experiments was conducted that showed that the TLNS solutions are sensitive to the value of the explicit numerical

smoothing. This can be seen in Fig. 4, where the variation of the surface skin friction coefficient c_f, evaluated on the windward symmetry plane at the rear of the cylindrical portion of the body ($x = 1.130$ ft), is shown as a function of the coefficient of the smoothing term ϵ_e. Reducing the fourth-order smoothing caused c_f to increase toward the levels predicted by the PNS code and the experimental measurements. A numerical smoothing constant value of $\epsilon_e = 0.010$ gave the best results for this case and was chosen as the desired value for all additional computations.

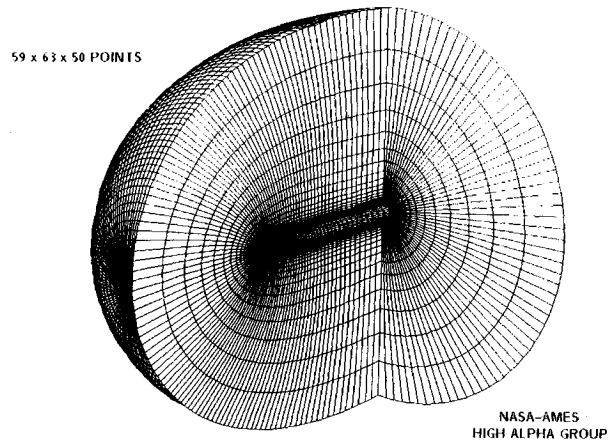

Fig. 3 Tangent ogive-cylinder grid.

Comparison Between Parabolized Navier-Stokes and Thin-Layer Navier-Stokes Results

Typical results obtained for the ogive cylinder at $\alpha = 6.3$ and 10.4 deg are shown in Figs. 5–7. Boundary-layer velocity profiles at three circumferential positions ($\phi = 120$, 150, and 180 deg) at $\alpha = 6.3$ deg are shown in Figs. 5. Both codes give similar results and are in good agreement with measured data.[21] Figure 6 presents the computed and measured circumferential surface pressure distributions on the rear of the cylindrical portion of the body ($x = 1.130$ ft). Again, both codes give nearly identical results, and both are in close agreement with the experimental measurements.

Computed surface flow patterns obtained for the ogive cylinder at $\alpha = 10.4$ deg with the PNS and and TLNS codes are shown in Figs. 7. The computed flow patterns are in very close agreement, and both show the development of primary crossflow separation starting approximately two thirds down

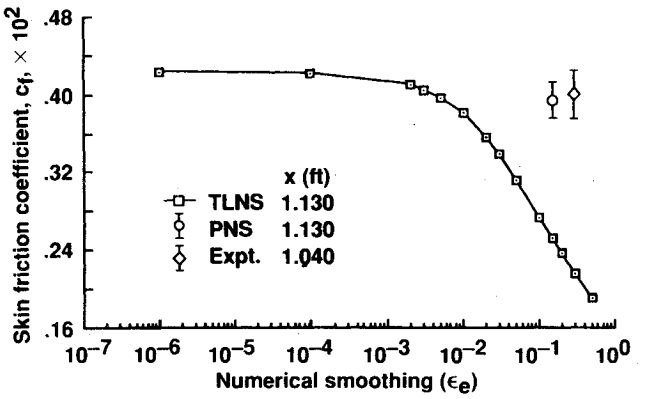

Fig. 4 Skin friction coefficient variation with smoothing constant: $M_\infty = 3.0$; $\alpha = 4.2$ deg.

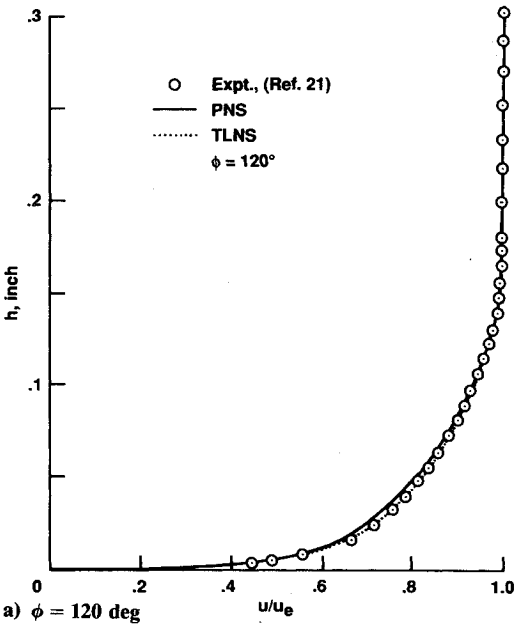

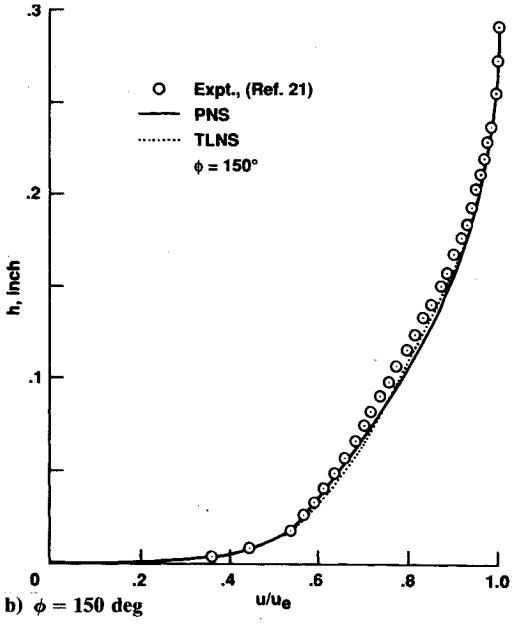

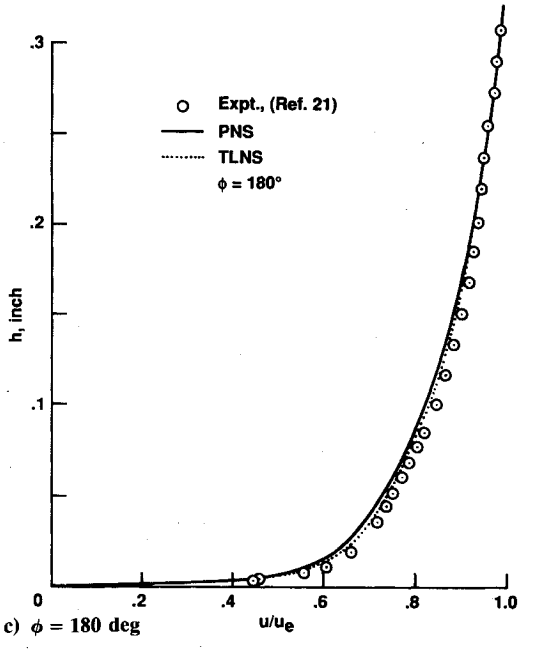

Fig. 5 Boundary-layer velocity profiles: $M_\infty = 3.0$; $\alpha = 6.3$ deg; $x = 1.13$ ft.

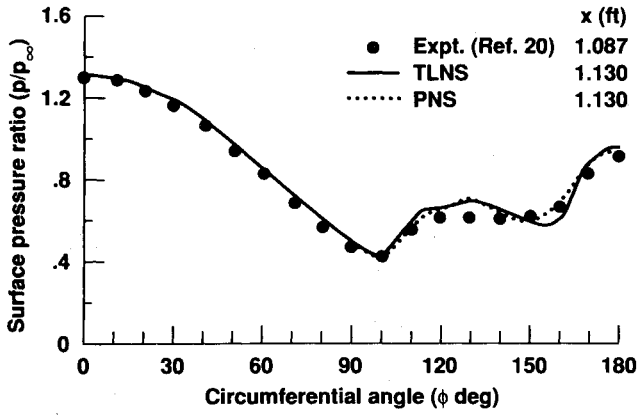

Fig. 6 Circumferential surface pressure distributions: $M_\infty = 3.0$; $\alpha = 10.4$ deg; $x = 1.13$ ft.

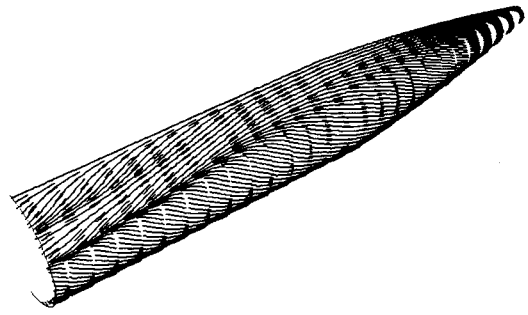

a) Results from PNS code

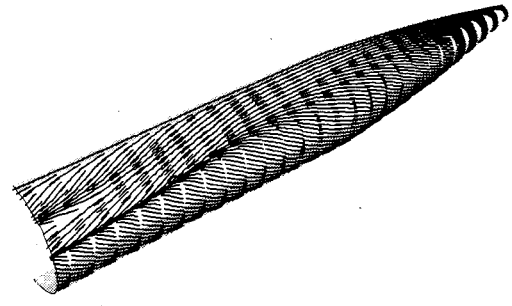

b) Results from TLNS code

Fig. 7 Computed surface oil flow: $M_\infty = 3.0$; $\alpha = 10.4$ deg; $Re_D = 1.216 \times 10^6$.

the body, and secondary crossflow separation that develops approximately 1 body diameter from the aft end of the cylinder. These results demonstrate the ability of the TLNS code to accurately predict separated flows on bodies at moderate angles of attack.

Subsonic High-Incidence Flow

A series of flows was computed about a tangent ogive-cylinder body in subsonic flow using the TLNS code to investigate the differences in the computed flow structure between laminar and turbulent high-incidence flow and to illustrate the improvements in turbulent flow results due to the modified turbulence model. The body had a 3.5-diameter tangent ogive forebody with a cylindrical afterbody extending aft of the nose-body junction for 7.0 diameters. This body geometry had been extensively tested by Lamont[22] in the NASA Ames Research Center 12-Ft Pressure Wind Tunnel, where detailed surface pressure distributions were obtained at Reynolds numbers ranging from $Re_D = 2 \times 10^5$ to 4.0×10^6 and at angles of attack ranging from $\alpha = 20$ to 90 deg. The grid used for the numerical predictions of the flow about the body was shown in Fig. 3. The flow was assumed to be symmetric, and a plane of symmetry was imposed. Except as noted later, the grid consisted of 59 axial, 50 radial, and 63 circumferential points.

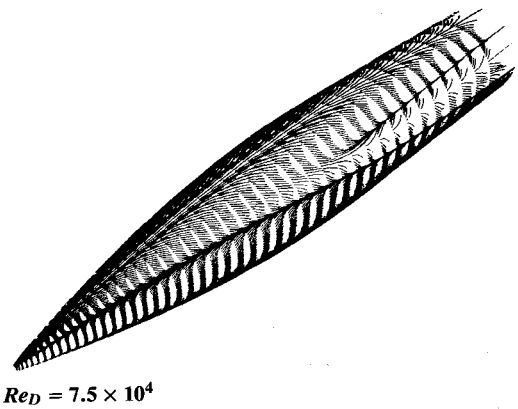

a) $Re_D = 7.5 \times 10^4$

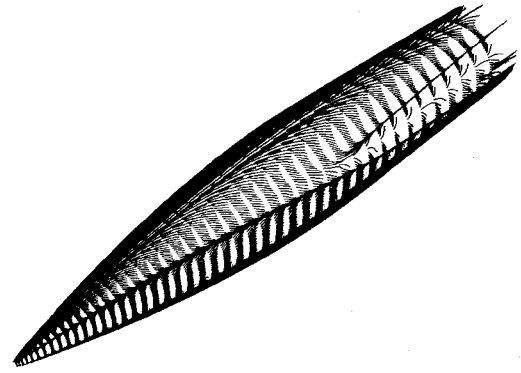

b) $Re_D = 2 \times 10^5$

Fig. 8 Computed surface oil flow: $M_\infty = 0.2$; $\alpha = 20$ deg (laminar).

Laminar Flow

In order to give perspective to the comparison between the two turbulence models, two computations were carried out for laminar flow over the tangent ogive-cylinder body. The flow was computed for $M_\infty = 0.2$ and $\alpha = 20$ deg for two Reynolds numbers, $Re_D = 7.5 \times 10^4$ and 2×10^5. The computed surface flow pattern over the forward portion of the body ($0 \leq x/D \leq 6.3$) for $Re_D = 7.5 \times 10^4$ is presented in Fig. 8a. The surface flow pattern shows a well-established primary crossflow separation line emanating from the nose tip and running the length of the body. A secondary crossflow separation originates upstream of the ogive-cylinder junction ($x/D \approx 2.9$) as the adverse circumferential pressure gradient increases. Note that the primary crossflow separation line is located approximately 90 deg from the windward symmetry plane. The surface flow pattern for the $Re_D = 2 \times 10^5$ case was reported previously[23] and is shown in Fig. 8b. As can be seen from comparing the surface flow patterns, there are only small differences between the two laminar computations.

Laminar vs Turbulent Flow

Computations were carried out to predict turbulent flow about the tangent ogive-cylinder body at $M_\infty = 0.2$, $\alpha = 20$, 25, and 30 deg, and $Re_D = 5.0 \times 10^6$. Except as noted, these computations were done using the modified turbulence model.[10,11] The computed surface flow patterns and the corresponding helicity density contours for $\alpha = 20$ deg are presented in Figs. 9. Helicity density has been found to be an excellent method of visualizing the position and strength of vortices.[24] Helicity density, the scalar product of the local velocity and vorticity vectors, indicates both the strength and sense of rotation of the vortices. Thus, helicity density contours give more flow information than either pressure or density contours. Notice the growth of the primary vortices and the downward movement of the primary vortex separation line with increasing axial distance along the length of the body, consistent with the surface flow pattern. Also, the secondary vortex separation region becomes apparent near the end of the body.

Several differences can be observed between the laminar and turbulent flows. In the laminar flow, the primary crossflow separation occurs closer to the windward symmetry plane than in the turbulent flow. On the cylinder portion of the body, the laminar primary crossflow separation occurs at $\phi \approx 90$ deg, in contrast to $\phi \approx 120$ deg for the turbulent case. This effect is well known from previous experimental investigations of high-incidence body flow and occurs because the turbulent viscous layer has higher momentum due to increased mixing with the outer inviscid flow. Thus, it can better negotiate the adverse circumferential pressure gradient it encounters on the leeward side of the body. As a consequence, the laminar primary crossflow vortices are more widely spaced and extend further above the body than in the turbulent flow. Analogously, in the laminar case, the induced flow on the leeward side of the body is more sensitive to the adverse circumferential gradient caused by the primary vortices. Thus, in general, the laminar secondary crossflow separation line is further displaced circumferentially from the primary crossflow separation than in the turbulent flow. As seen in Figs. 8 and 9a, the laminar secondary separation line starts further down the body than in the turbulent case.

Effect of Turbulence Model Modifications

To again demonstrate the improvements that the modified turbulence model yields in the prediction of high-incidence turbulent flow about bodies, computations were carried out for turbulent flow about the tangent ogive-cylinder body at $\alpha = 20$ deg using the original Baldwin-Lomax[15] model. Surface flow patterns obtained with the unmodified model are presented in Fig. 10a, whereas the corresponding helicity density contours are presented in Fig. 10b.

A comparison of the surface flow patterns for the original and modified turbulence models (Figs. 9a and 10a) shows that the primary crossflow separation line predicted with the modified model is located lower circumferentially than the one predicted with the original model. Furthermore, the results obtained with the modified model show the development of a tertiary separation line near the rear of the body. The helicity density contours (Figs. 9b and 10b) illustrate the differences clearly, as the original model yields a simple vortex roll-up structure, whereas the modified model shows a larger, more complex structure. This is consistent with previous experience[10] in computing supersonic high-incidence turbulent flow, where it was found that the original model tends to wash out the details in the separated flow region. This is due to the inability of the original turbulence model to distinguish between the off-surface flow structures and the underlying attached turbulent boundary layers in determining the viscous length scale in regions of crossflow separation. The modified model gives more realistic results since the full structure of the separation region is accounted for.

Effect of Grid Resolution

The choice of a computational grid for any flowfield computation is dependent on the scale of the flow structures that must be resolved. For high-angle-of-attack flows, adequate resolution must be provided for the attached viscous layers and for the details of the leeward-side vortex structure. For the turbulent cases studied, the grids consisted of 50 nonuniformly spaced points in the radial direction between the body and the outer boundary. The radial stretching was chosen to give a value of y^+ between 3 and 4 at the first point above the body surface at all locations. This had been found necessary to properly resolve the viscous layer flow characteristics for a turbulent boundary layer.[9]

The need for adequate circumferential grid resolution for accurate prediction of flow physics at high angles of attack can be seen by examining the surface flow pattern for $\alpha = 20$ deg obtained with 63 circumferential points ($\Delta\phi = 3$ deg)

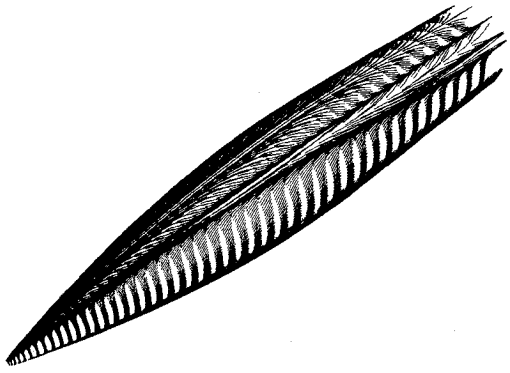

Fig. 9a Computed surface oil flow: $M_\infty = 0.2$; $\alpha = 20$ deg; $Re_D = 5.0 \times 10^6$ (turbulent).

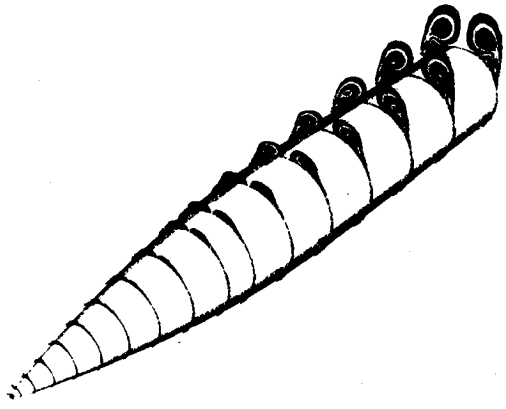

Fig. 9b Helicity density: $M_\infty = 0.2$; $\alpha = 20$ deg; $Re_D = 5.0 \times 10^6$ (turbulent).

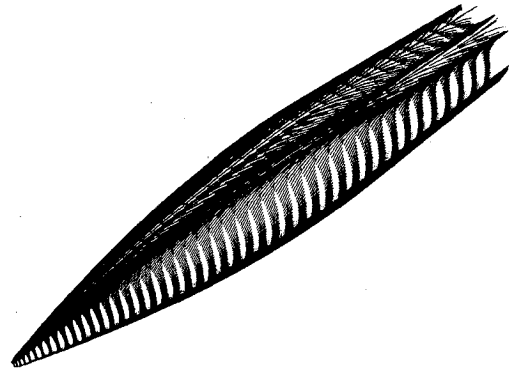

Fig. 10a Computed surface oil flow: $M_\infty = 0.2$; $\alpha = 20$ deg; $Re_D = 5.0 \times 10^6$ (unmodified Baldwin-Lomax model).

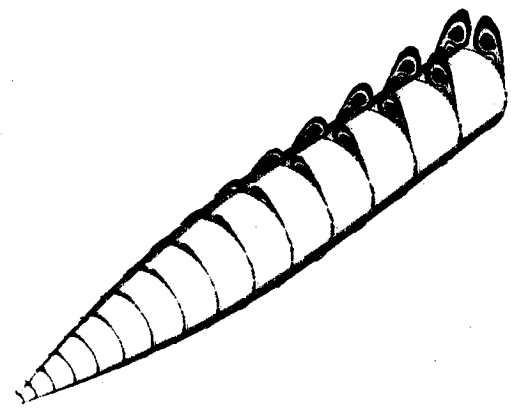

Fig. 10b Helicity density: $M_\infty = 0.2$; $\alpha = 20$ deg; $Re_D = 5.0 \times 10^6$ (unmodified Baldwin-Lomax model).

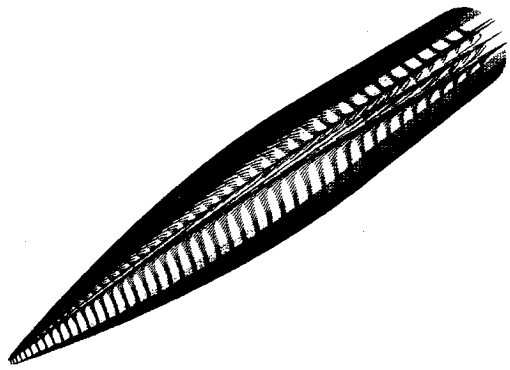

Fig. 11a Computed surface oil flow: $M_\infty = 0.2$; $\alpha = 20$ deg; $Re_D = 5.0 \times 10^6$ (turbulent, with doubled circumferential resolution).

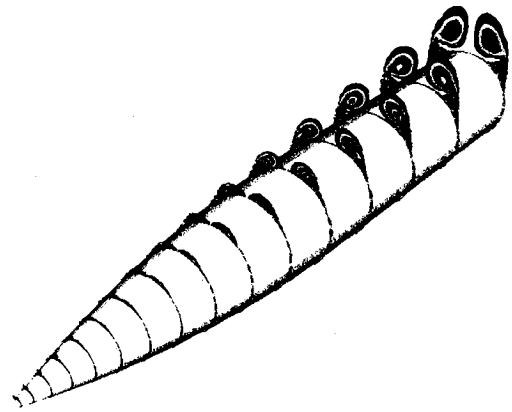

Fig. 11b Helicity density: $M_\infty = 0.2$; $\alpha = 20$ deg; $Re_D = 5.0 \times 10^6$ (turbulent, with doubled circumferential resolution).

shown in Fig. 9a. The primary and secondary crossflow separation lines are circumferentially closely spaced on the ogive portion of the body. As a result, the code had trouble in differentiating between the two crossflow separations. In Fig. 9a, the primary crossflow separation line originating at the nose tip seems to become the secondary crossflow separation line on the aft part of the body. This is physically unrealistic, as the vortices from the primary separation have the opposite sense of rotation than those coming from the secondary separation line. Repeating the computation with double the circumferential resolution (123 circumferential points, $\Delta\phi = 1.5$ deg) cured the problem. The computed surface flow pattern obtained with the finer grid spacing is shown in Fig. 11a, and the primary crossflow separation line runs the length of the body. The corresponding helicity density contours are shown in Fig. 11b (compare with Fig. 9b).

The requirement for increased circumferential grid resolution, which was apparent at $\alpha = 20$ deg, is significantly reduced as the flow physics are altered with changing angle of attack. The surface flow patterns computed with $\Delta\phi = 3$ deg at $\alpha = 25$ deg are shown in Fig. 12a, while those obtained for 30 deg are shown in Fig. 12b. Note that in both of these cases the primary crossflow separation line originates at the nose and is continuous, whereas the secondary crossflow separation originates downstream. The primary separation line moves circumferentially down the side of the body as the angle of attack increases due to the higher adverse pressure gradient that is encountered. At the same time, the stronger primary vortices cause the secondary separation to occur closer to the leeward symmetry plane, thus increasing the circumferential spacing between the primary and secondary lines. As a result, fewer grid points are required to resolve the salient features of the flow. Our experience suggests that at least four or five circumferentially spaced grid points are required between separation lines in order to realistically model the flowfield.

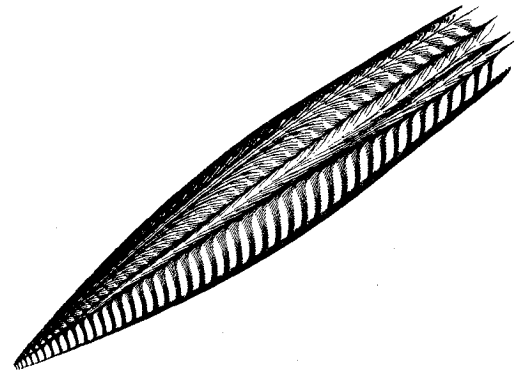

a) $\alpha = 25$ deg

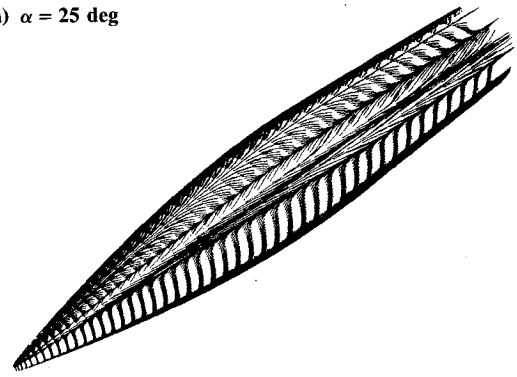

b) $\alpha = 30$ deg

Fig. 12 Computed surface oil flow: $M_\infty = 0.2$; $Re_D = 5.0 \times 10^6$ (turbulent).

Comparison with Experiment

In order to validate the numerical predictions, a comparison between the computed results and experimental data[22] is made. Figures 13 show computed and measured circumferential surface pressure distributions at five axial locations ($x/D = 0.5$, 2.0, 3.5, 5.0, and 6.0) for $M_\infty = 0.2$ and $\alpha = 20$, 25, and 30 deg. The experimental measurements obtained on both the left and right side of the body are shown to indicate any asymmetries that may occur in the flowfield. Notice that, at $\alpha = 20$ deg, the surface pressure measurements are relatively symmetric at all locations along the length of the body. However, significant asymmetries exist for $\alpha = 25$ and 30 deg at the rear of the body ($x/D = 5.0$ and 6.0).

There are three predictions shown for $\alpha = 20$ deg (Fig. 13a), those computed for the base grid and circumferentially doubled grid at $Re_D = 5 \times 10^6$ and a solution computed in the base grid at $Re_D = 4 \times 10^6$. Note that the predictions for the two Reynolds numbers show no significant differences, even at the aft end of the body on the leeward side. However, the grid with the doubled circumferential does show some differences and seems to predict the pressure rise on the leeward side of the body better than the baseline grid. This result confirms the conclusions based on the surface oil flows for the same case, as was shown previously (see Figs. 10). These results help to confirm the notion that the turbulence model crossflow correction is valid for both subsonic and supersonic flows,[25] as the modified model has been shown to reasonably predict pressure distributions for this body geometry. Although the computed flow patterns show secondary and tertiary separation lines (see Figs. 9a and 11a), and the predicted pressures also show this behavior, the experimental results do not seem to show the existence of such flow features. However, this is probably due to the relative coarseness of the pressure measurements, which do not allow strong conclusions to be made as to the existence of the finer features of the flow. Keener[26] has reported experimental surface oil flows for similar bodies, which show secondary crossflow separation lines and give confidence that the secondary (and possibly tertiary) separation lines are being properly predicted.

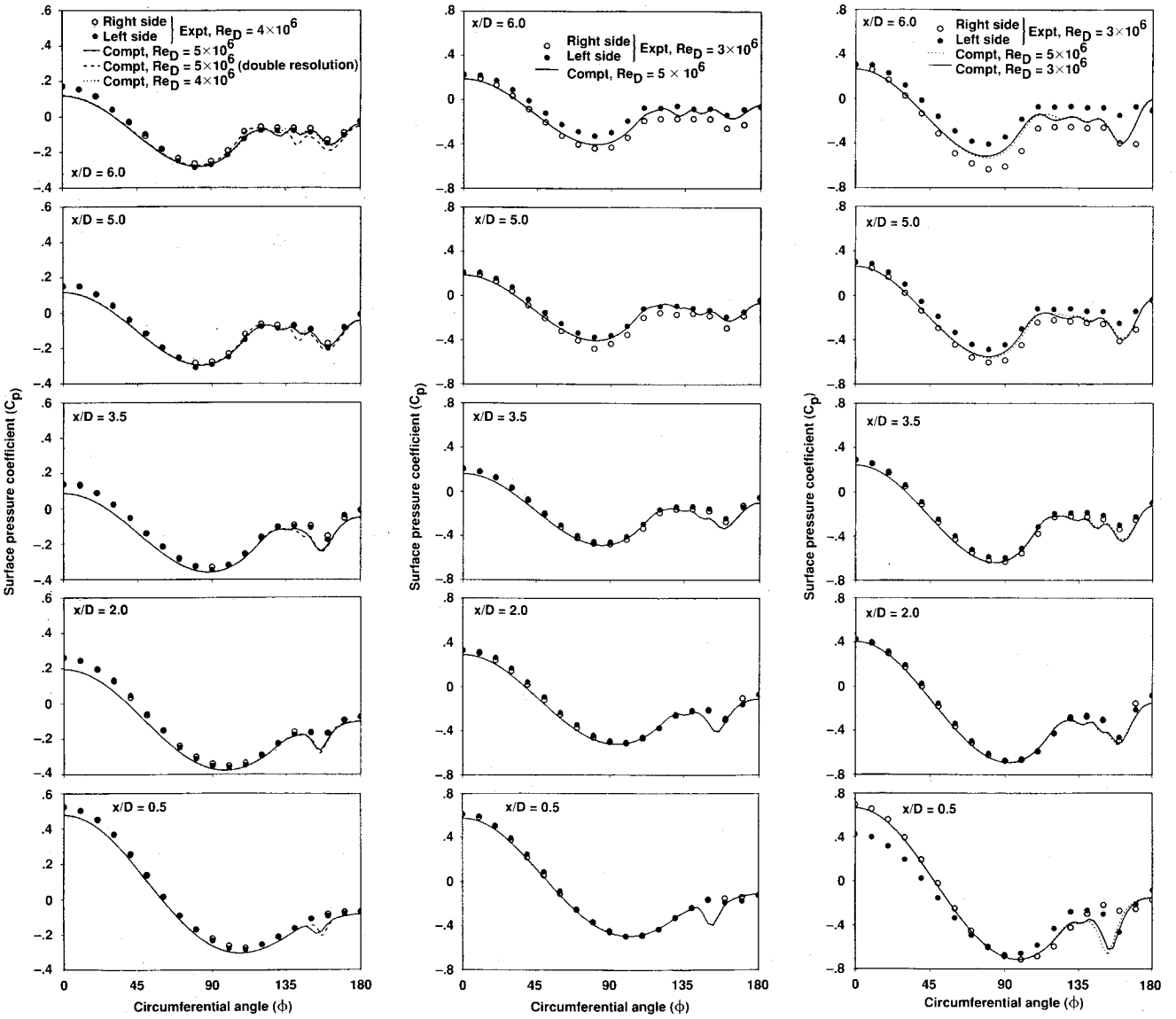

a) $\alpha = 20$ deg b) $\alpha = 25$ deg c) $\alpha = 30$ deg

Fig. 13 Circumferential surface pressure distribution: $M_\infty = 0.2$.

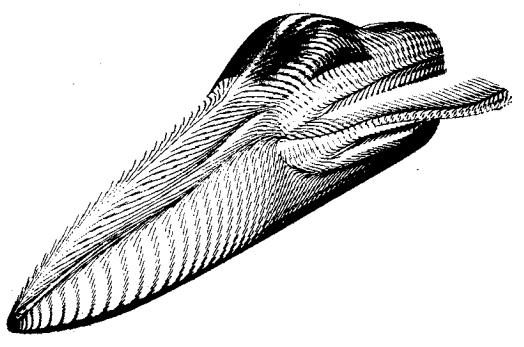

Fig. 14a Computed surface oil flow: $M_\infty = 0.2$; $\alpha = 30$ deg; $Re_{\bar{c}} = 11.52 \times 10^6$ (turbulent).

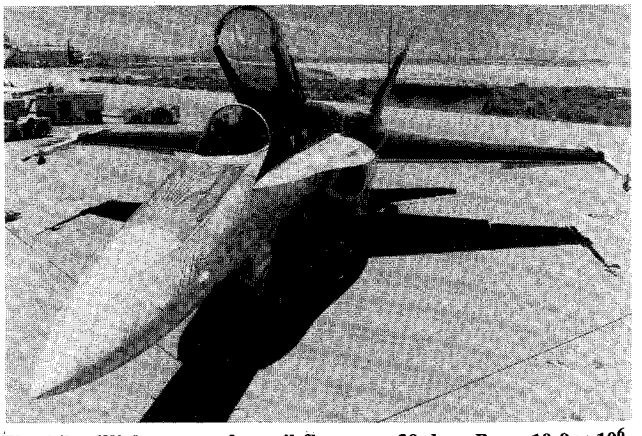

Fig. 14b Flight test surface oil flow: $\alpha = 30$ deg; $Re_{\bar{c}} = 10.9 \times 10^6$.

Figures 13b and 13c present data for $\alpha = 25$ and 30 deg, respectively. Two computations are shown for $\alpha = 30$ deg, both computed in the base grid, one at $Re_D = 5 \times 10^6$ and the other at $Re_D = 3 \times 10^6$ (matching the experimental data). Again, the effect of Reynolds number on the predicted pressures is insignificant, even at the most rearward stations. Note that although the predictions are for the symmetric case, and only half the flowfield was computed, they fall between the measured pressures that are asymmetric near the aft end of the body ($x/D = 5.0$ and 6.0). In spite of the complex flow structure, the predictions are in good agreement with the experimental data, as long as the flow is symmetric.

F-18 Results

The previous results are now applied to a complex geometry at high angle of attack. The lessons learned on the ogive-cylin-

der bodies, such as the effects of numerical smoothing, turbulence modeling, and grid resolution, are applied to compute flow about an F-18 fighter fuselage forebody. The predictions are made for subsonic flow, $M_\infty = 0.2$, at $\alpha = 30$ deg, and a Reynolds number matching flight, $Re_{\bar{c}} = 11.52 \times 10^6$ (turbulent flow).

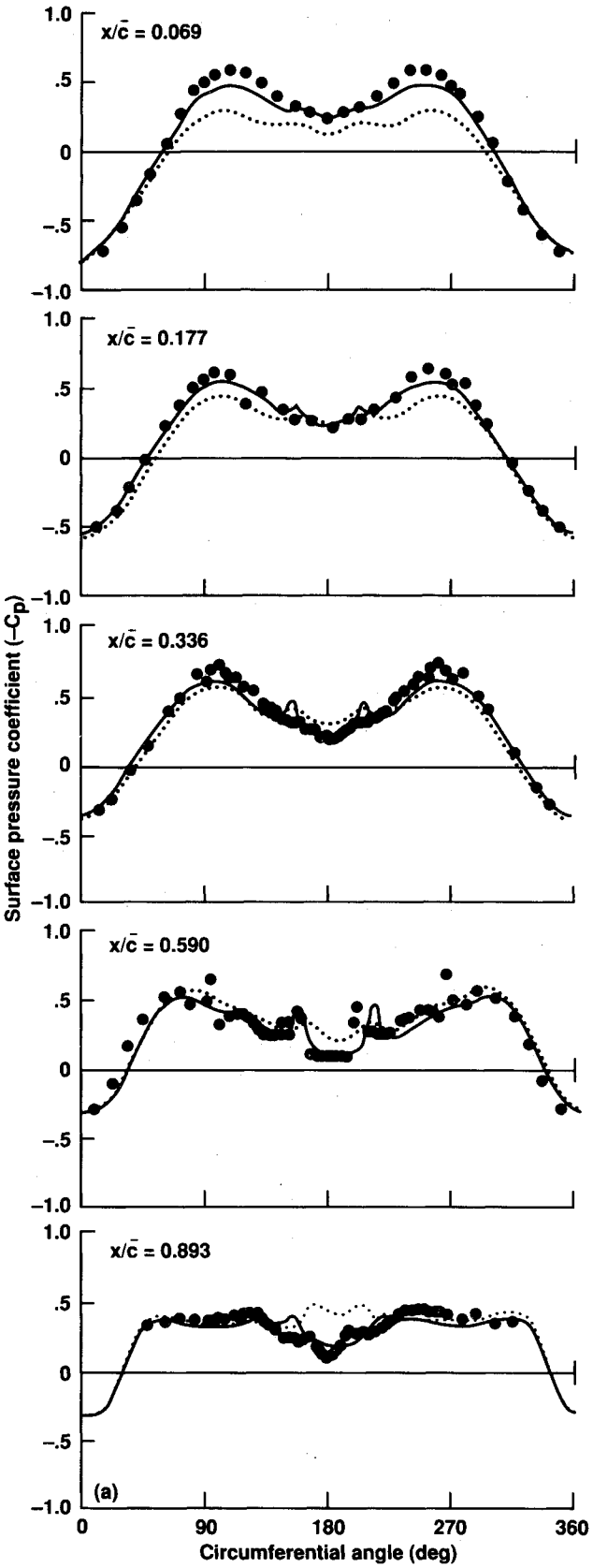

Fig. 15a Surface pressure predictions compared with flight test data on forebody: $\alpha = 30$ deg.

The F-18 geometry was modeled using a two-block grid structure, with the forward block extending from the nose tip to the origin of the wing leading-edge extension (LEX) and the aft block ending at the beginning of the wing. The forward block consists of 36 axial, 53 circumferential, and 50 radial grid points, whereas the aft block consists of 35 axial, 85 circumferential, and 50 radial grid points. The zonal boundary contains one-to-one matching of grid points, with the extra circumferential grid points in the second block being used to define the LEX. The radial spacing was chosen to give a $y^+ \approx 5$ at the first point above the body surface. In addition, a one-block grid structure was used for some predictions.

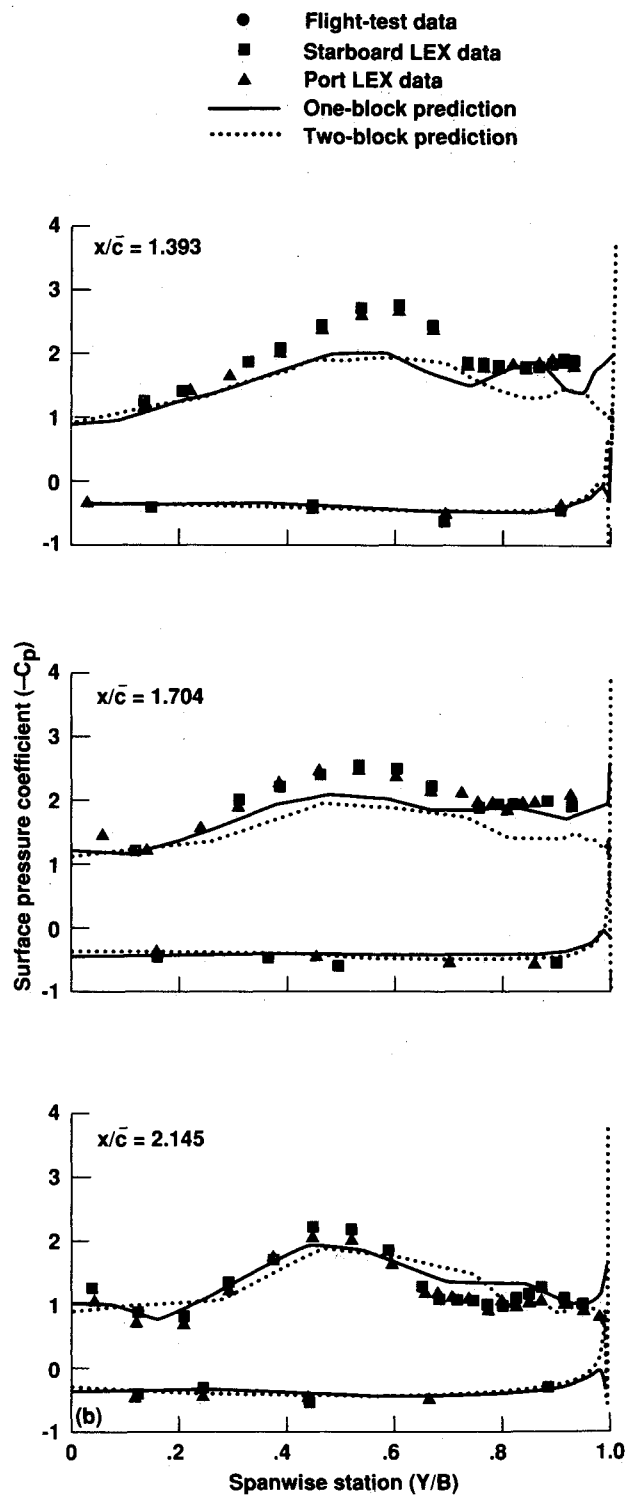

Fig. 15b Surface pressure predictions compared with flight test data on LEX: $\alpha = 30$ deg.

The computed surface flow pattern is presented in Fig. 14a and may be compared with the surface flow visualization photo that was taken from flight tests currently being conducted at NASA Ames Dryden Flight Research Facility,[27] presented in Fig. 14b. The predictions are in good agreement with the flight test data, especially for the position of the primary and secondary separation lines along the forebody and the secondary crossflow separation line along the LEX. In addition, a crossflow separation line is observed on the fuselage under the LEX. This separation is due to the increased adverse circumferential pressure gradient caused by the LEX, and is displaced circumferentially downward as the LEX grows in size.

Previously reported computations[28,29] of surface pressures are compared with flight test measurements in Figs. 15. The predictions are for five axial stations of the fuselage forebody ($x/\bar{c} = 0.069$, 0.177, 0.336, 0.590, and 0.893), as well as three axial locations of the LEX ($x/\bar{c} = 1.393$, 1.704, and 2.145). The predictions were made with both the one-block and two-block grids (see Refs. 28 and 29 for further details). The fuselage forebody predictions show the ability of the crossflow separation turbulence models to predict surface pressures for a body at high angles of attack. The surface pressure predictions for the LEX are compared with experimental data taken on both the starboard and port LEX, which show a level of asymmetry in the flowfield. Although the LEX predictions do not compare as well with the experimental data as those for the fuselage forebody, it should be noted that these predictions are for an isolated forebody. The addition of the wing and aft fuselage geometries, with their associated upwash fields, should improve the pressure predictions on the LEX.

IV. Conclusions

High-angle-of-attack flows have been numerically predicted using a thin-layer Navier-Stokes code. Predictions have been made for supersonic flow over a secant ogive cylinder that show good agreement with surface pressures and boundary-layer velocity profiles, as well as with previously computed parabolized Navier-Stokes predictions. Subsonic predictions for a tangent ogive cylinder at high incidence were also found to be in good agreement with available experimental data. In order to show the ability of the numerical methods to compute high-angle-of-attack flow over a more complex geometry, predictions were presented for the subsonic flow over the F-18 fuselage forebody.

Several factors have been found to have a large impact on the ability to accurately predict high-angle-of-attack flow. Although some of these factors were reported in a previous work, they have been applied to new geometries with complex three-dimensional and time-dependent flowfields. This gives more confidence in the ability of the thin-layer Navier-Stokes code to accurately predict the features of high-incidence flow. Numerical smoothing must be used with caution in order to insure that the physical nature of the predictions is not perturbed, leading to inaccurate results with dubious physical meaning. The turbulence model must account for the complex vortical structures found in the highly separated flow region. The modifications to the turbulence model shown in this work were developed specifically for three-dimensional crossflow separation, making it possible to accurately predict high-incidence flow. Finally, the grid spacing must be judiciously chosen in order to insure that the salient surface and off-surface features of the flow are resolved. Future investigations into the importance of these, and other, factors will help to improve the prediction of the complex vortical structures found in high-angle-of-attack flow.

Acknowledgments

The authors wish to thank Robert M. Hall of the NASA Langley Research Center for his help in supplying the experimental pressure coefficients measured in Lamont's experiments. We would also like to thank Ken Gee for his assistance in preparing the graphical representations of the computed flows.

References

[1]Fujii, K., and Obayashi, S., "Computations of Three-Dimensional Viscous Transonic Flows Using the LU-ADI Factored Scheme," Japanese National Aerospace Laboratory, TR-889T, 1985.

[2]Newsome, R. W., and Adams, M. S., "Numerical Simulation of Vortical-Flow over an Elliptical-Body Missile at High Angles of Attack," AIAA Paper 86-0559, Jan. 1986.

[3]Pan, D., and Pulliam, T. H., "The Computation of Steady Three-Dimensional Separated Flows over Aerodynamic Bodies at Incidence and Yaw," AIAA Paper 86-0109, Jan. 1986.

[4]Kordulla, W., Vollmers, H., and Dallmann, U., "Simulation of Three-Dimensional Transonic Flow with Separation Past a Hemisphere-Cylinder Configuration," *Applications of Computational Fluid Dynamics in Aeronautics,* AGARD CPP-412, Paper 31, April 1986.

[5]Ying, S. X., Schiff, L. B., and Steger, J. L., "A Numerical Study of Three-Dimensional Separated Flow Past a Hemisphere-Cylinder," AIAA Paper 87-1207, June 1987.

[6]Fujii, K., and Schiff, L. B., "Numerical Simulation of Vortical Flows Over a Strake-Delta Wing," AIAA Paper 87-1229, June 1987.

[7]Vatsa, V. N., Thomas, J. L., and Wedan, B. W., "Navier-Stokes Computations of Prolate Spheroids at Angle of Attack," AIAA Paper 87-2627, Aug. 1987.

[8]Hartwich, P. M., and Hall, R. M., "Navier-Stokes Solutions for Vortical Flows Over a Tangent-Ogive Cylinder," AIAA Paper 89-0337, Jan. 1989.

[9]Schiff, L. B., and Sturek, W. B., "Numerical Simulation of Steady Supersonic Flow Over an Ogive-Cylinder-Boattail Body," AIAA Paper 80-0066, Jan. 1980.

[10]Degani, D., and Schiff, L. B., "Computation of Supersonic Viscous Flows Around Pointed Bodies at Large Incidence," AIAA Paper 83-0034, Jan. 1983.

[11]Degani, D., and Schiff, L. B., "Computation of Turbulent Supersonic Flows Around Pointed Bodies Having Crossflow Separation," *Journal of Computational Physics,* Vol. 66, No. 1, 1986, pp. 173–196.

[12]Schiff, L. B., and Steger, J. L., "Numerical Simulation of Steady Supersonic Viscous Flows," *AIAA Journal,* Vol. 18, No. 12, 1980, pp. 1421–1430.

[13]Steger, J. L., Ying, S. X., and Schiff, L. B., "A Partially Flux-Split Algorithm for Numerical Simulation of Unsteady Viscous Flows," *Proceedings of a Workshop on Computational Fluid Dynamics,* University of California, Davis, CA, 1986.

[14]Viviand, H., "Conservative Forms of Gas Dynamics Equations," *La Recherche Aérospatiale,* No. 1, 1974, pp. 65, 66.

[15]Baldwin, B. S., and Lomax, H., "Thin Layer Approximation and Algebraic Model for Separated Turbulent Flows," AIAA Paper 78-0257, Jan. 1978.

[16]Steger, J. L., "Implicit Finite-Difference Simulation of Flow About Arbitrary Two-Dimensional Geometries," *AIAA Journal,* Vol. 16, No. 7, 1978, pp. 679–686.

[17]Steger, J. L., and Warming, R. F., "Flux Vector Splitting of the Inviscid Gasdynamic Equations with Applications to Finite-Difference Methods," *Journal of Computational Physics,* Vol. 40, No. 2, 1981, pp. 263–293.

[18]Ying, S. X., "Three-Dimensional Implicit Approximately Factored Schemes for Equations in Gasdynamics," Ph.D. Dissertation, Stanford Univ., Stanford, CA, June 1986.

[19]Cebeci, T., Smith, A. M. O., and Mosinkis, G., "Calculation of Compressible Adiabatic Turbulent Boundary Layers," *AIAA Journal,* Vol. 8, No. 11, 1970, pp. 1974–1982.

[20]Reklis, R. P., and Sturek, W. B., "Surface Pressure Measurements on Slender Bodies at Angle of Attack in Supersonic Flow," U.S. Army Ballistic Research Laboratory, ARBRL-MR-02877, Aberdeen Proving Ground, MD, Nov. 1978.

[21]Kayser, L. D., and Sturek, W. B., "Experimental Measurements in the Turbulent Boundary Layer of a Yawed, Spinning Ogive-Cylinder Body of Revolution at Mach 3.0. Part II. Data Tabulation," U.S. Army Ballistic Research Laboratory, ARBRL-MR-02813, Aberdeen Proving Ground, MD, March 1978.

[22]Lamont, P. J., "The Complex Asymmetric Flow Over a 3.5D Ogive Nose and Cylindrical Afterbody at High Angles of Attack," AIAA Paper 82-0083, Jan. 1982.

[23]Schiff, L. B., Degani, D., and Gavali, S., "Numerical Simulation of Vortex Unsteadiness on Slender Bodies of Revolution at Large Incidence," AIAA Paper 89-0195, Jan. 1989.
[24]Levy, Y., Seginer, A., and Degani, D., "Graphical Representation of Three-Dimensional Vortical Flows by Means of Helicity Density and Normalized Helicity," AIAA Paper 88-2598, June 1988.
[25]Degani, D., Schiff, L. B., and Levy, Y., "Numerical Prediction of Subsonic Turbulent Flows over Slender Bodies at High Incidence," *AIAA Journal* (to be published).
[26]Keener, E. R., "Flow-Separation Patterns on Symmetric Forebodies," NASA TM 86016, Jan. 1986.
[27]Fisher, D. F., and Meyer, R. R., "Flow Visualization Techniques for Flight Research," NASA TM 100455, Oct. 1988.
[28]Schiff, L. B., Cummings, R. M., Sorenson, R. L., and Rizk, Y. M., "Numerical Simulation of High-Incidence Flow over the F-18 Fuselage Forebody," AIAA Paper 89-0339, Jan. 1989.
[29]Cummings, R. M., Rizk, Y. M., Schiff, L. B., and Chaderjian, N. M., "Navier-Stokes Predictions of the Flowfield Around the F-18 (HARV) Wing and Fuselage at Large Incidence," AIAA Paper 90-0099, Jan. 1990.